Till Strothteicher and Nicolas Fezans; Combined Design of Gain-Scheduled C-Star and Maneuver Load Alleviation Laws
Journal of Guidance, Control, and Dynamics 2026 49:7, 2097-2109
doi: 10.2514/1.G009267

Combined Design of Gain-Scheduled C-star and Maneuver Load Alleviation Laws

Till Strothteicher [*] and Nicolas Fezans[†]
German Aerospace Center (DLR), Institute of Flight Systems, 38108, Braunschweig, Germany

This paper presents an automated tuning of a longitudinal baseline load factor flight augmentation system (FAS) and a maneuver load alleviation (MLA) controller. The FAS is representative of those employed in modern fly-by-wire civil aircraft (regarding the pull-up maneuver loads) and the MLA function reduces sizing loads. These control laws are applied to a flexible and energy-efficient aircraft. During the iterative aeroelastic optimization of the preliminary aircraft design, the evolution of the aircraft design and structure call for an adjustment of the control system tuning. An optimization-based procedure is proposed to fully automate the multi-objective control tuning process, which would allow considering their load reduction performance in an automated multidisciplinary optimization loop of the aircraft. The parameters of the active control functions are scheduled over the equivalent air speed and Mach number using a candidate function to capture the change of the elevator authority. The closed-loop FAS shows good tracking of the pilot command over the entire flight envelope. The MLA function effectively alleviates the worst case maneuver vertical bending moment throughout the wingspan as well as the entire flight envelope. Adding an input filter and a center of gravity scheduling law decreases the wing root bending moment further.

Nomenclature

Symbols

c	=	Local chord length
$C_{m,\alpha}$	=	Aerodynamic moment coefficient derivative with angle of attack
δ	=	Deflection
Δ	=	Change from trim-value
η_R	=	Tuning requirement performance
t_d^*	=	Dimensionless deflection time
T_s	=	Sampling time

[*]Research Scientist, Department of Flight Dynamics and Simulation, till.strothteicher@dlr.de, Corresponding Author
[†]Scientific Advisor, Department of Flight Dynamics and Simulation, nicolas.fezans@dlr.de

$T_{\circ \rightarrow \square}$ = Transfer function from $\circ$ to $\square$

V_∞ = Undisturbed onflow velocity

x_{CG} = Longitudinal center of gravity position

X = Analysis point

Subscripts, Superscripts

$\square^e$ = Error

$\square^I$ = Integral

$\square^P$ = Proportional

$\square^{ref}$ = Reference

$\square_E$ = Elevator

$\square_{cmd}$ = Command

$\square_{co}$ = Crossover

$\square_{hf}$ = High frequency

$\square_{lf}$ = Low frequency

$\square_{reL}$ = Lift redistribution

$\square_{trig}$ = Trigger

I. Introduction and Motivation

The aeroelastic design process of modern aircraft concepts involves sizing the aircraft based on ultimate or design loads plus a safety factor (typically 1.5 or less, cf. for instance [1, Appendix K]). Ultimate or design loads of wings are partly defined based on the limit loads for specific load cases (e.g., gust, turbulence, and maneuver loads). Alleviation of the gust and maneuver loads offers potential for lightweight construction and/or improved aerodynamic efficiency via higher aspect-ratio wings. The Sustainable and Energy-Efficient Aviation (SE^2A) Cluster of Excellence* investigates numerous technologies for sustainable and eco-friendly air transport systems. Among the cluster's research activities are concepts for load reduction in conjunction with tools for the (pre-) design of aircraft.

Usually, for the inboard (and heaviest) portion of the wing, sizing loads are defined by the gust and maneuver loads [2]. Without specific control functions, the maneuver loads tend to dominate the other loads. However, it is straightforward to reduce them by deflecting wing surfaces (ailerons, spoilers) upward to shift the lift distribution inboard when the load factor in the fuselage exceeds a certain threshold. This way, the maneuver loads can be reduced below the peak load levels of open-loop gust encounters. Numerous studies have investigated the potential for mass savings through the use of active maneuver load alleviation control in the last fifty years. Early works by White [3], Allison et al. [2], and Johnson et al. [4] have shown this potential as well as the trade-off between reducing the structural

*https://www.tu-braunschweig.de/en/se2a

weight and improving the aerodynamic efficiency of the aircraft by increasing the wing span.

In comparison, gust loads are much more challenging to alleviate as the sizing gusts are usually of very large amplitude and the control surfaces have limited authority and deflection rates. With the use of lidar sensors that detect gusts/turbulence slightly ahead of the aircraft, reductions on the order of 15–20% of the maximum values can be reached while remaining strictly within the position and rate limits of the control surface actuators [5], compared to about 5–7% without lidar sensors but with aggressive (high-gain) and much less robust controllers. Methods for designing active gust load alleviation (GLA) controllers with and without lidar sensors have been designed and applied to the considered aircraft configuration (cf. section III) by the authors' research group, cf. for instance [6], as well as other research groups, e.g., [7]. This paper presents methods to design both a flight augmentation system (FAS) and a maneuver load alleviation (MLA) function to complement the already available GLA controllers. Their design is automated as much as possible so that they can eventually be incorporated into the multidisciplinary optimization of the aircraft.

Integrating load alleviation functions at the aircraft pre-design stage has already been proposed by several groups, e.g. [8–12], and is expected to become standard in the next decade. With each iteration of the aircraft design loop, properties affecting the aeroelastic and flight dynamic behavior of the aircraft are changed, which also calls for an update of the various active control functions. In turn, these adapted control functions impact the gust and maneuver load envelopes of the aircraft for which the aircraft structure is sized. To be able to run design loops efficiently and to consider the active control functions while optimizing the aircraft, the control synthesis for the different modes must be automated. The fine tuning of these control functions usually involves fairly complex and time-consuming trade-offs, which can hardly be reproduced in such automated schemes. The intention is therefore not to design the final controllers. Rather, controllers are tuned whose performance is representative of modern longitudinal flight control laws (and not overly optimistic) with respect to the loads. This guides the multidisciplinary optimization into an appropriate region of the design space, allowing the optimizer to leverage the knowledge of load reduction performance without the risk of using too optimistic load reduction levels for the current design as the achieved load performance is monitored and regularly evaluated during the optimization.

The remaining sections are structured as follows: Section II provides an overview of relevant prior work on both the design and tuning of FAS control laws based on the vertical load factor n_z and on MLA functions. After introducing the considered aircraft in Section III, the proposed control design methods are presented in Section IV. Results obtained with the tuned controllers are discussed in Section V. Finally, Section VI summarizes this work and provides an outlook.

II. Relevant Prior Work

A. Baseline Control Law

Given the widespread adoption of n_z-based control laws, there are surprisingly few references on the tuning of such laws. The Airbus A320 normal law is documented in [13]. Regarding automated tuning, nonlinear dynamic inversion (NDI) laws are often considered as a means to force the aircraft to behave like a specific reference model. However, these approaches can lead to an aggressive controller with very fast closed loop poles and with large actuation levels to force the aircraft to match the reference model's behavior. NDI can however be a solution, if used properly, and can also provide significant added value when the aircraft exhibit a nonlinear behavior, as shown in [14, 15]. Overall, the three references from Airbus [13, 14, 16], published over a period of 19 years, exhibit the same control law structure. The more recent publication, however, delves deeper into the adaptation of the parameters with changes to the flight point and the flight phase as well as the compensation of nonlinear effects.

The existing literature on non-automated tuning of load factor-based control laws is also limited, both regarding the structure of the law and its tuning. Much of the research work focuses on the handling qualities of the longitudinal motion, assuming a bare and rigid aircraft with no significant FAS (stability augmentation at most, but no command augmentation). Two examples of in-depth investigation of active control systems and their impact on the aircraft longitudinal dynamics as well as the resulting handling qualities can be found in [17, 18]. Without FAS, the poles and zeros of the transfer function from the elevator deflection to the load factor n_z determine both the dynamic response to pilot inputs and the disturbance rejection properties. For such non-augmented aircraft, there is a direct link between stick input response and disturbance rejection capabilities. Hence, the handling quality criteria defined in terms of short-period pole location[†] considered both aspects. Using pole placement techniques would make a lot of sense when tuning a few controller gains which do not change the open-loop behavior too drastically. Reference [14, 19] mentions explicitly that a pole placement approach is used to tune the feedback gain, but also mentions that further filters are required to cope with flexible modes (ride comfort, no coupling with flutter).

Flight augmentation controllers may, as is already the case with an n_z-law, yield a decoupling between disturbance rejection properties and response to stick inputs. As already mentioned, they can include filters and significantly increase the order of the closed-loop dynamic system. As a consequence, the simple notion of having a short-period pair of poles that largely define the longitudinal handling qualities may be invalidated. The fact that the link between the pole-zero map and the handling qualities cannot be readily established for highly control-augmented aircraft does not prevent, however, the disturbance rejection and reference (i.e., stick input) tracking properties from being tuned so that good handling qualities are obtained. By adding and tuning a feedforward filter to the pilot command input, the aircraft

[†] The lower bound on the frequency (typically 2 rad/s) can be interpreted as a minimum disturbance rejection bandwidth. The upper-bound on the frequency (typically 2.4–2.6 rad/s) prevents excessively forward center of gravity locations which would cause a deficit in the maneuverability of the aircraft ($C_{m,\alpha}$ too strongly negative). A minimum damping ratio (typically 0.5–0.7) is specified to prevent a large resonance at the short-period mode frequency.

response can be tuned independently from the feedback gains and disturbance rejection characteristics of the system [14, section 4].

In the following, a similar baseline control law structure and requirements are considered, however the tuning will be performed and automated utilizing frequency-based methods. Such methods were also applied to a baseline controller in [20]. The current work is largely based on [21], with some modifications and significant additions.

B. Maneuver Load Alleviation Function

The references [8–12], mentioned earlier for their investigation of the load alleviation and mass saving potentials, propose a series of MLA configurations. For the design of MLA functions, the basic idea is to shift the wing lift inboard by deflecting the outboard control surfaces (ailerons and spoilers) upward and sometimes also inboard control surfaces (high speed ailerons and flaps) downward. For civil airliners, maneuvers are usually performed at relatively low frequencies and, if properly handled, interaction between MLA functions and flexible modes can largely be avoided. It is, for instance, common to cut (filter out) the pilot commands above the frequency of the first flexible modes of the airplane for comfort reasons and for preventing biodynamic coupling. The prevention of such interaction is not directly considered in this work. The evaluations made at the end of the paper consider dynamic maneuvers and not only the quasi-static pull-up/ push down maneuvers specified in [1, §331 b)].

III. Considered Aircraft Model

A. Aircraft Configuration

The aircraft considered in this work is the SE^2A Mid-Range (MR) Aircraft [22]. Its top-level aircraft design requirements are similar to an Airbus A320-200. The mission profile of the SE^2A MR is optimized to balance direct operating costs and CO_2-equivalent emissions [6]. In order to reduce contrail-emissions, the nominal mission profile is lower and slower than that of an A320-200. This mission profile led to a lower wing sweep angle. Additionally, both the wingspan and the aspect ratio are larger in comparison, while the wing loading is lower. One of the unconventional design features of this aircraft is the use of over-wing turbofan engines, with the engine inlet very close to the upper surface of the wing and a very aft position of the engine, see Figure 1. The aerodynamic benefits of such engine arrangements are being investigated by other groups in the SE^2A cluster. This feature has some impact on the aeroelastic behavior of the aircraft, but has fairly little impact on the work presented in this paper as the following baseline and MLA controller are mostly active at frequencies below the first flexible modes of the aircraft.

The wing structure of the SE^2A MR is sized to maneuver loads only. Gust loads are neglected in the structural sizing of the wing based on the assumption that a gust load alleviation system, e.g., the one from [6], reduces the gust loads down to the maneuver loads. The structural sizing was performed twice: first with the load envelope corresponding to a 2.5 g pull-up maneuver and then also for 2.0 g. The latter case yields an operational empty mass difference of two percent [23]. This indicates the mass reduction potential that can be obtained using an MLA function, which ensures that the closed loop load envelope remains within the open loop load envelope obtained for a 2.0 g pull-up maneuver.

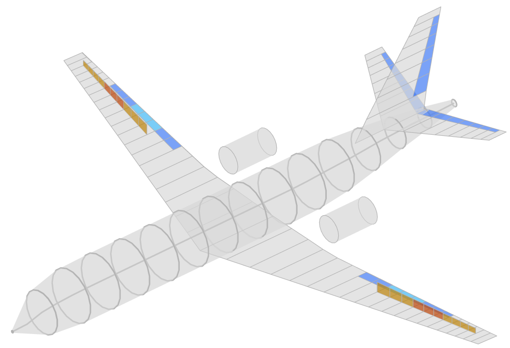

Fig. 1 SE²A Mid-Range Aircraft, primary control surfaces in blue, load alleviation devices in orange

B. Nonlinear Model

The nonlinear aeroelastic flight dynamics model (FDM) documented in [23] is utilized for simulation of the given energy-efficient passenger airplane. The flexible structural model is based on a high-order finite-element model. Cut loads are computed at 134 load stations throughout the structure using the mode displacement method. The aerodynamics are implemented via a mid-fidelity unsteady model consisting of an unsteady airfoil model, dynamic stall model, and spanwise downwash model. The coupling of aerodynamics and structural dynamics is realized by handling the aerodynamic forces over to the flexible-body equations of motion [24] and feeding the resulting structure geometry back to the aerodynamic model.

Actuators are modeled as second-order systems with nonlinear limits on both deflection and deflection rate (20 deg and 40 deg/s for the elevator). Due to the low torsional stiffness of the wings, the outboard ailerons have very little control authority at high dynamic pressure. Instead, the micro-tabs presented in [25] are used in this work as load alleviation devices (LAD) on the wing. They work similarly to spoilers, i.e., their deflection reduces lift locally by causing flow separation. Unlike conventional spoilers, micro-tabs do not rotate relative to the wing surface. Instead, they move perpendicular to it, like the air brake of a glider, and their deflection is expressed as a percentage of the local chord length %c. Their maximum deflection is 2%c, and their spanwise location reaches from 81.7% to 95.3% of the wing half span, see Figure 1. They are positioned at 60%c in chord direction, providing good control authority on the local lift and low impact on the local pitching moment of the wing (and thus indirectly on wing torsion) [25]. Micro-tabs, like spoilers, can only reduce local lift, so they are not applicable for MLA during push-down maneuvers.

At this stage of the work, a steady aerodynamic model of the micro-tabs is considered, with a similar deflection rate limit to that of classical spoilers. This limit is imposed to ensure that the effectiveness and responsiveness of the micro-tabs is not over-estimated. For spoilers, the dimensionless deflection speed t_d^* is defined as:

$$t_d^* = t_d \frac{V_\infty}{c} \tag{1}$$

where t_d denotes the deflection time, V_∞ the undisturbed freestream velocity, and c the local chord length. Rapid deflection of spoilers leads to an instantaneous lift increase, followed by the intended lift reduction [26]. This phenomenon is also known as the spoiler adverse lift effect and does not occur for $t_d^* > 5...8$ (see [26, 27]). The limitation regarding the micro-tab deflection rate derived from the spoiler adverse lift effect is introduced in section IV.B and is assumed to be more restrictive than the mechanical deflection rate limit of the micro-tabs actuator.

C. Linear Model Processing

The simulation framework allows trimming, linearizing, and simulating the aircraft throughout the flight envelope. In this work the nonlinear flight dynamics/aeroelastic model is trimmed and linearized at the 72 flight points shown in Figure 2. Two mass cases are considered: maximum take-off weight (MTOW) and maximum zero-fuel weight (MZFW). Whilst not defined as different mass cases in the following, an additive variation of the center of gravity (CG) position is also considered for each flight point and mass case (default position and offset forwards by ±2%MAC). In total, 432 linear models are generated. For the controller tuning process, the flight points marked with purple crosses in Figure 2 with MTOW and standard CG position are utilized. Solely the longitudinal dynamics are considered: Lateral dynamics are truncated based on the assumption that they are decoupled from the longitudinal dynamics. This assumption holds for wing-level steady state flight with negligible roll and sideslip angle/rate [28, 29], and symmetrical mass cases.

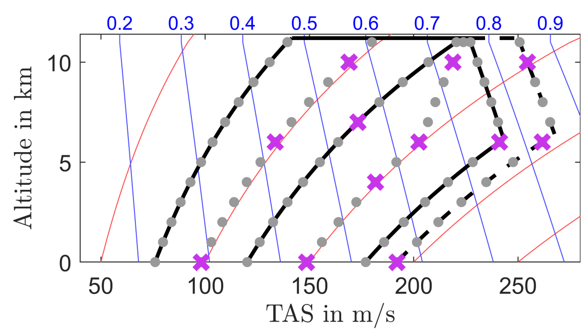

Fig. 2 Flight envelope: from sea level up to service ceiling and from stall speed V_{s1g} to maneuver velocity V_A to cruise speed V_C up to dive velocity V_D (vertical black lines), constant Mach number along blue lines, constant EAS along red lines, linear models available at all markers

The full-order linear models have 800 states. Reduced models are computed for the controller design by means of a Hankel singular value-based truncation. Prior to the computation of the Hankel singular values, the model outputs are equalized based on the steady-state response to the considered inputs. Some outputs (e.g., wing root bending moment $WRBM$ in Nm) are several orders of magnitude larger than others (e.g., Θ in deg, q in deg/s, or n_z in g) and would otherwise dominate the transfer function, resulting in an unbalanced reduced-order model quality (good match of the largest outputs, but poor match of the others). The resulting state-space models of the aircraft:

$$\boldsymbol{G_{AC}}: \begin{aligned} \dot{\boldsymbol{x}} &= \boldsymbol{A}\boldsymbol{x} + \boldsymbol{B}\boldsymbol{u} \\ \boldsymbol{y} &= \boldsymbol{C}\boldsymbol{x} + \boldsymbol{D}\boldsymbol{u} \end{aligned} \tag{2}$$

have a state vector $\boldsymbol{x}$ with 75 states. The inputs $\boldsymbol{u} = [\delta_{E,cmd}, \delta_{LAD,in,cmd}, \delta_{LAD,mid,cmd}, \delta_{LAD,out,cmd}]^{\mathrm{T}}$ are the commanded elevator deflection and commanded load alleviation device deflection. All control surfaces are deflected symmetrically (i.e., on both wings). The outputs $\boldsymbol{y} = [n_z, q, V_{xz}, \Theta, WRBM, \delta_E, \dot{\delta}_E, \delta_{LAD}, \dot{\delta}_{LAD}]^{\mathrm{T}}$ are the vertical load factor, pitch rate, combined longitudinal and vertical inertial velocity in body-fixed frame (true airspeed), pitch angle, wing root bending moment, elevator deflection and deflection rate, as well as the LAD deflection and deflection rate. The outputs n_z, q, V_{xz} and Θ relate to rigid-body aircraft movement at the CG. The linear models are converted to discrete time (using a zero-order hold method) to obtain a realistic flight control system with a sampling time T_s of 25 ms (sampling rate 40 Hz). Delays such as sensor delays, computational delays and transmission delays are assumed to sum up to 50 ms. They are applied as input delays at all plant inputs.

IV. Control Design

This section presents the baseline control law and the MLA controller as well as their tuning. These control functions are tuned with a structured H_2/H_∞ method at the twelve design points (highlighted as purple crosses in Figure 2) with MTOW and default CG position. Controller parameters related to the elevator are scheduled over the Mach number and EAS to capture the effects of compressibility and dynamic pressure on the elevator effectiveness. The aerodynamic effectiveness of the trailing edge flaps model can be approximated as a quadratic function of EAS and Mach number [23, 30]. Hence, a continuously scheduled gain is parameterized as

$$K(\boldsymbol{p}) = \left[1, EAS, EAS^2, \mathrm{Ma}, \mathrm{Ma}^2\right] \boldsymbol{p}^T \tag{3}$$

where the tunable parameters

$$\boldsymbol{p} = [p_0, p_{EAS}, p_{EAS2}, p_{Ma}, p_{Ma2}] \tag{4}$$

are tuned for each controller gain individually. After tuning, the candidate function is evaluated for the EAS and Mach number of the current flight point, yielding a smooth gain-scheduling. Results for individual and combined controllers as well as further insight into the control design are presented in Section V.

The MATLAB `systune` framework [31] is utilized for the automated tuning process of both baseline and MLA controller. It allows for structured H_2/H_∞ control law synthesis, i.e., a control structure with fixed-order control elements can be defined a priori. The framework employs a non-smooth optimization technique [32], which efficiently and effectively handles large order systems (recall 75 states for the design system). However, the lower-order controller may correspond to a local optimum. It is therefore common practice to repeat the control synthesis with random start values to try to achieve a more favorable optimum (closer to the global optimum).

Tuning requirements are defined using H_2/H_∞ norms. The `systune` framework allows tuning requirements to be classified as either `hard` or `soft`. `Soft` requirements are minimized (e.g., load reduction objective), subject to `hard` requirements being met (e.g., actuator limits and stability requirements). The H_2/H_∞ norms are applied here only to single-input single-output (SISO) transfer functions. The H_∞ norm of a transfer function is its largest gain for a sinusoidal input across all frequencies. An H_∞ requirement is formulated by multiplying the SISO transfer function with a frequency-dependent weighting function and constraining the H_∞ norm of the augmented transfer function to an upper bound. The requirement is met if its performance η_R, i.e., the norm of the augmented transfer function, is smaller than one. The inverse of the weighting function, also known as a template, is denoted as $W^{-1}(s)$ and is used as an upper bound on the non-augmented transfer function. The same logic applies to H_2 requirements, however this norm can be interpreted in the time domain for SISO systems in two ways [33]. From a stochastic viewpoint, it is interpreted as the root mean square (RMS) value of the output due to an unit-intensity white noise input. From a deterministic point of view, it is interpreted as the energy of the output in response to a unit impulse input.

A. Design of the Baseline Control Law

As already understood for decades and used by Airbus since the A320 generation [13], letting pilots control the flight path angle γ or rather adjusting it by means of a load factor command (Δn_z is proportional to $\dot{\gamma}$) reduces their workload considerably. Indeed, pilots are less focused on stabilizing the flight path and correcting it in the presence of disturbances, as the control law handles this for them. Instead, they act as an outside-loop guidance law deciding on the required flight path. This fundamentally changes the role of the pilots, relieving them of low-level control tasks.

At high speed, minor angle of attack variations (and thereby also pitch rate) are sufficient to cause large variations of the load factor. However, at low speed, the range of load factor variations is more limited and pilots were found to rather rely on the pitch rate [34, 35]. This observation led to considering a mix of the load factor at the pilot station $\Delta n_{z,pilot}$ and the pitch rate q for specifying the desired response to pilot stick inputs. This mixed signal is called C^* (C-star) and is defined as:

$$\Delta C^* = \Delta n_{z,pilot} + \frac{V_{co}\, q}{g} = \Delta n_z + \frac{l_{pilot}\, \dot{q}}{g} + \frac{V_{co}\, q}{g} \tag{5}$$

The load factor at the pilot station is affected by the CG load factor Δn_z, pitch acceleration $\dot{q}$, and distance from CG to cockpit l_{pilot} (for a rigid aircraft). The crossover velocity $V_{co} = 122\,\mathrm{m/s}$ defines the velocity above which C^* is dominated (in steady-state) by the $\Delta n_{z,pilot}$ term [34].

Upper and lower bounds on the time-domain step response of C^* are used to judge the longitudinal stick response of the control law. This performance criterion only focuses on the input-output relationship, i.e., does not specify disturbance rejection properties, but can be applied to high-order aircraft models (e.g., including aeroelasticity, actuator and sensor dynamics, and loop delays) and with complex control laws [35]. Figure 3 shows the baseline controller structure, which is based on [13, 14, 20]. The C^* controller is implemented in discrete time and tracks the reference load factor commanded by the pilot Δn_z^{ref}.

The feedback path is primarily used for model error correction and disturbance rejection. It consists of an integral load factor tracking feedback controller with the scheduled gain $K_{n_z}^I(\boldsymbol{p})$ as well as proportional pitch rate and load factor feedback with the scheduled gains $K_q^P(\boldsymbol{p})$ and $K_{n_z}^P(\boldsymbol{p})$. The feedforward path $K^{FF}(\boldsymbol{p})$ is used to accelerate the closed-loop response to pilot inputs.

Both the tracking error output n_z^e as well as the `analysisPoints` X_q and X_{n_z} are employed during the tuning process. `analysisPoints` are used as inputs and outputs at the given location in the control loop. Note that an `analysisPoint` is utilized to identify a location in the diagram that is of interest for specific analyses or to express some design specifications, without actually modifying the model. In the signal flow direction, an `analysisPoint` first outputs the signal and then allows an input to be added. X_q and X_{n_z} are placed on the feedback signals and used to specify the stability margins. X_{n_z} is also used to define the output sensitivity function on the load factor n_z, with which a disturbance rejection specification is expressed. There are five `hard` tuning requirements for the baseline control law, which are summarized in Table 1 and explained in the following.

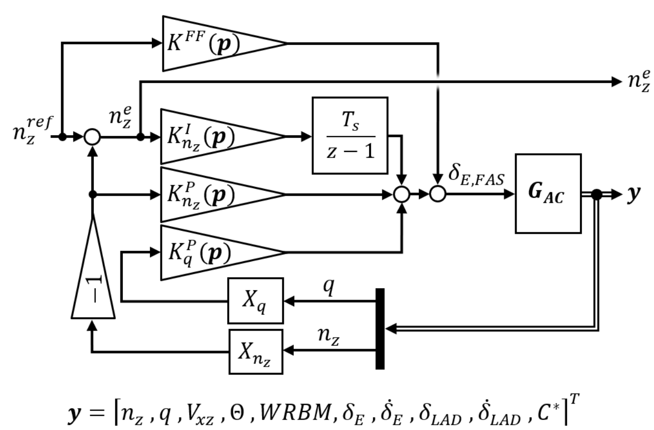

Fig. 3 Baseline controller structure

Table 1 Baseline controller tuning goals

Goal	Description	Type	Location	Target
		Hard Requirements		
1)	n_z^{ref} Tracking	H_∞	$T_{n_z^{ref} \to n_z^e}$	$\leq W_{e,n_z}^{-1}(z)$ (Adjusted during tuning)
2)	n_z Tracking Overshoot	H_∞	$T_{n_z^{ref} \to n_z}$	$\leq 10\%$
3)	Feedback stability margin	`Margin`	X_q, X_{n_z}	≥ 6 dB|45 deg
4)	Disturbance Rejection	H_∞	X_{n_z}	$\leq W_{reject}^{-1}(z)$
5)	Elevator deflection rate	H_∞	$T_{n_z^{ref} \to \dot{\delta}_E}$	$\leq \dfrac{40 \text{ deg/s}}{\Delta n_{z,feas}/3}$

1. Reference Load Factor Tracking

For reference tracking, the magnitude of the closed loop transfer function $T_{ref \to e}$, where ref is the reference input and e is the tracking error, must be low at low frequencies. To accelerate the system response, an overshoot of the tracking signal is usually allowed. For good noise suppression, the closed loop system should show little response to the tracking error at high frequencies. These demands are achieved by shaping $T_{ref \to e}$ with an H_∞ requirement. Figure 4 visualizes the associated tracking error template. It is defined as a band-pass filter:

$$W_e^{-1}(s) = \frac{e_{Peak}\, s + \omega_{hpf}\, e_{lf}}{s + \omega_{hpf}} \frac{(e_{hf}/e_{Peak})\, s + \omega_{lpf}}{1 + \omega_{lpf}} \tag{6}$$

with low frequency error e_{lf}, peak error e_{Peak}, high frequency error e_{hf}, high-pass filter cutoff frequency $\omega_{hpf} = 2/t_{resp}$, response time t_{resp}, low-pass filter cutoff frequency $\omega_{lpf} = 2/(t_{resp}(1 - 1/\kappa_{reso}))$, and the width of the resonance window in which an increased tracking error is allowed κ_{reso}.

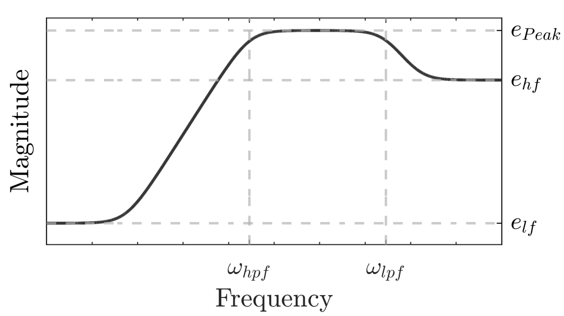

Fig. 4 Schematic tracking error template $W_e^{-1}(s)$

The reference tracking error template for the baseline controller $W_{e,n_z}^{-1}(z)$ is defined by Eq. (6), with $e_{lf} = 10^{-6}$ and

$e_{hf} = 1.01$. Choosing $e_{Peak} = 3$ and $\kappa_{reso} = 2.2$ leads to an allowed tracking error of 6 dB at the closed loop resonance frequency.

It is not straightforward to select the response time for a closed loop system constrained by a set of H_2/H_∞ requirements. Thus, an iterative approach is adopted: a tunable control structure along with its requirements is passed to `systune`. If the control synthesis fails to converge to a controller that satisfies all `hard` requirements ($\max\{\eta_R^{hard}\} > 1$) after n_{rand} random restarts, the tracking requirement is relaxed by increasing the response time until a satisfactory solution is reached, see Algorithm 1. The initial response time is chosen low enough that Algorithm 1 fails on its first iteration to ensure that the quickest closed loop response satisfying all requirements is achieved. For the given application the load factor tracking error template $W_{e,n_z}^{-1}(z)$ is initiated with a response time of 600 ms. The permissible response time $t_{resp,max}$ is defined a priori to limit the number of iterations. Further requirements are presented below.

Algorithm 1 Control synthesis with iterative tracking performance relaxation

while $\max\{\eta_R^{hard}\} > 1 \quad \&\& \quad t_{resp} < t_{resp,max}$ **do**

Increase response time t_{resp} by 5%

Update tracking error template $W_e^{-1}(s)$

Synthesize a controller using `systune` with n_{rand} random restarts

end while

2. Load Factor Tracking Overshoot

In accordance with the design rules of baseline controllers at Airbus [16, 36], and to meet the C^* step response boundaries, the overshoot of the load factor should not exceed 10%. This is applied via an H_∞ constraint on the transfer function from reference load factor input (n_z^{ref}) to load factor output (n_z). Note, that the H_∞ norm of the transfer function is used as an overshoot estimate based on the analogy to second-order model characteristics.

3. Stability margins

A stability margin requirement is applied to provide robustness against system uncertainties. Classical stability margins are measures of variations in gain or phase that can be tolerated whilst maintaining closed-loop stability [37]. Classical gain and phase margins $GM|PM$ of at least 6 dB|45 deg are specified at the `analysisPoints` X_q and X_{n_z} in Figure 3. To further ensure robustness against simultaneous variations in gain and phase, disk margins are employed in the tuning process instead of classical margins. The classical margin specification is translated to an unskewed disk with radius $\alpha = 2\max\{(GM-1)/(GM+1), tan(PM/2)\}$, which serves as a lower bound on the disk margin of the corresponding SISO loop. The latter is defined as $2\left(||(1-L(s))(1+L(s))^{-1}||_\infty\right)^{-1}$, where $L(s)$ denotes the open-loop transfer function (recall the `analysisPoint` description) [31, 37]. Note that this only applies to unskewed disk margins of SISO loops. These stability margin requirements are realized using the `Margin` requirement (feature of `systune`).

4. Disturbance and Model Error Rejection

The reference tracking might largely be achieved via a feedforward filter. However, real-world systems differ from their models considered during tuning. To ensure that the remaining model error is compensated in a timely manner, some minimum level of rejection must be provided by the feedback controller. The effect of output disturbances and multiplicative output uncertainty is specified using the closed loop transfer function at point X_{n_z} (cf. Figure 3). A minimum output disturbance rejection bandwidth ω_{DRB} of 0.5 rad/s and a maximum output disturbance rejection peak DRP of 5 dB are required [38, 39]. By specifying a high-pass filter with the same characteristics

$$W_{reject}^{-1}(s) = \frac{s\,DRP}{s + \omega_{DRB}\sqrt{2(DRP)^2 - 1}} \tag{7}$$

as an H_∞ template, a minimum disturbance / model error rejection is ensured.

5. Limit on Elevator Commands

It is highly advisable to tune the controller such that it complies with actuator deflection and deflection rate saturation limits. Reaching the saturation limits may result in degraded closed-loop performance or even loss of stability (in the case of feedback control). To prevent saturation of the elevator actuator deflection rate, the H_∞ norm of the transfer function from the reference input (n_z^{ref}) to the actuator deflection rate output ($\dot{\delta}_E$) is constrained to the actuator deflection rate limit (40 deg/s) relative to one third of the largest expected reference input ($\Delta n_z^{ref} = \Delta n_{z,feas}/3$, where $\Delta n_{z,feas}$ is the maximum feasible load factor at the given flight point, determined by trimming the aircraft for maximum load factor up to 2.5 g). It is worth mentioning that this requirement does not generally restrict the controller from saturating the elevator actuator deflection rate. Rather, it ensures at the design points that $\dot{\delta}_E$ remains below 40 deg/s for sinusoidal reference inputs correlating with $\Delta n_{z,feas}/3$ pull-up maneuvers at all frequencies. Only a third of $\Delta n_{z,feas}$ is used here since the elevator rate limit must be maintained during normal operation. For sizing-relevant maneuvers, a rate limiter is implemented at the elevator input ensuring that the elevator rate stays below its limit. Like in [6], requirements are specified for the deflection rate only, since the deflections themselves are unlikely to reach their limits at the considered flight conditions.

B. Design of the Maneuver Load Alleviation Function

The MLA function is designed to reduce the inboard wing bending moment during maneuvers. This also reduces the design loads associated with the requirements for symmetrical maneuver conditions according to [1, §331]. These maneuvers (balanced, maximum pitch controller displacement, and checked maneuvers) are to be conducted with the maximum positive and negative load factors (defined by [1, §337]). Only the maximum positive load factor ($\Delta n_{z,feas}$, cf. section IV.A.5) is considered and shown in the following, for two reasons: Firstly, the design loads include the trim loads, so that upward bending moments, for example, are typically critical. Secondly, the selected LAD can reduce lift only, thus they are only effective, in terms of MLA, for large positive load factors.

The MLA function aims at mitigating the inboard bending moment by shifting the lift distribution towards the plane of symmetry of the aircraft. To achieve this, the MLA function consists of a nonlinear activation logic $\boldsymbol{MLA_{trig}}$ and a linear lift redistribution controller ($\boldsymbol{MLA_{LAD,reL}}$, $\boldsymbol{MLA_{E,reL}(p)}$), see Figure 5.

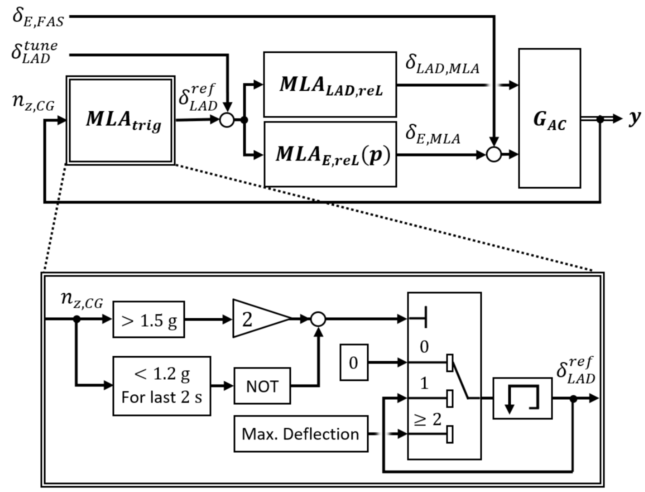

$$\boldsymbol{y} = \left[n_{z,CG}\,, q\,, V_{xz}\,, \Theta\,, WRBM, \delta_E\,, \dot{\delta}_E\,, \delta_{LAD}\,, \dot{\delta}_{LAD}\,, C^*\right]^T$$

Fig. 5 Maneuver load alleviation controller structure

$\boldsymbol{MLA_{trig}}$ feeds a reference LAD deflection δ_{LAD}^{ref} of 2%c (maximum LAD deflection) to the lift redistribution controller if Δn_z exceeds 0.5 g and deactivates if Δn_z stays below 0.2 g for more than two seconds. The waiting period is a safety feature to prevent coupling of the LAD deflection with buffeting effects or some flexible mode.

Once the MLA is activated, the outboard lift is reduced by deflecting the LAD. The desired flight path is maintained by compensating the ensuing lift reduction through a quasi-steady increase in angle of attack. That is, the elevator is deflected to both compensate the reduced lift and the change in pitching moment through the LAD deflection. Such a reconfiguration was also applied in [40]. LAD and elevator commands are provided dynamically to prevent transitory effects which affect the ride comfort [21].

$\boldsymbol{MLA_{LAD,reL}}$ defines the LAD command for the outboard lift reduction. It is a discrete-time second order system that is constant throughout the flight envelope. The damping ratio must be selected large enough for little overshoot (to limit the velocity at which the LAD reaches its mechanical end-stop) and small enough for a quick transient response. The bandwidth is selected as a trade-off between the need for avoiding inducing oscillations through rapid lift changes on the outboard portion of wing (i.e., for which a low bandwidth is preferable) and the need for a sufficiently fast reduction of the bending moment through the inboard shift of the lift distribution, ideally by ensuring that the LAD reaches its settling value noticeably before the wing root bending moment reaches its peak value. A bandwidth of 7.5 rad/s and a damping ratio of 0.8 are selected as a compromise between these two criteria[‡].

$\boldsymbol{MLA_{E,reL}}(\boldsymbol{p})$ defines the elevator command for the angle of attack adjustment / moment compensation and is a tunable discrete-time second order system. Its damping ratio $\zeta_{E,MLA}(\boldsymbol{p})$, natural frequency $\omega_{n,E,MLA}(\boldsymbol{p})$ and scaling $mag_{E,MLA}(\boldsymbol{p})$ are `tunableSurfaces`, parameterized by Equation 3.

The lift redistribution controller is tuned utilizing the structure depicted in Figure 5. Its tuning process is defined by three requirements which are summarized in Table 2 and explained below. The MLA controller is tuned for individual and combined use of the LADs sections. The MLA is connected with the baseline controller via the elevator command from the latter $\delta_{E,FAS}$.

Table 2 Lift redistribution (MLA) controller tuning goals

Goal	Description	Type	Location	Target
		Soft Requirements		
1)	Low Disruption of desired Flight Path	H_∞	$T_{\delta_{LAD}^{ref} \to n_z}$	$\leq \frac{0.002g}{2‰c},\ \forall\,\omega < 10$ rad/s
		Hard Requirements		
2)	Ride Comfort	H_2	$T_{\delta_{LAD}^{ref} \to n_z}$	$\leq \frac{0.032g}{2‰c} W_k^{-1}$
3)	Elevator deflection rate	H_∞	$T_{\delta_{LAD}^{ref} \to \dot{\delta}_E}$	$\leq \frac{40\,\text{deg/s}}{2‰c}$

1. Low Disruption of Desired Flight Path

Once $\boldsymbol{MLA_{trig}}$ is active, it feeds a reference LAD deflection of 2‰c to the lift redistribution controller. During lift redistribution, the aircraft should remain on the desired flight path to provide minimal baseline controller disturbance. This is ensured by limiting the output Δn_z to 0.002 g at low frequency for the largest expected reference input (δ_{LAD}^{ref} = 2‰c) using a frequency-limited H_∞ requirement. It is defined as a `soft` requirement, meaning that the optimization

[‡]Based on linear pull-up maneuver simulations of the baseline closed-loop at all flight points and mass cases, provided that the MLA is activated if Δn_z exceeds 0.5 g.

minimizes the H_∞ norm of $T_{\delta_{LAD}^{ref}\rightarrow n_z}$ while meeting all `hard` requirements.

2. Ride Comfort

Closely related, ISO 2631-1 defines passenger comfort ratings for the frequency-weighted RMS vertical acceleration. The low order approximation of the weighting filter

$$W_k(s) = \frac{81.89s^3 + 796.6s^2 + 1937s + 0.1466}{s^4 + 80.00s^3 + 2264s^2 + 7172s + 21196} \tag{8}$$

developed in [41] is applied here. Since the stochastic interpretation of the H_2 norm of a SISO system is, by Parseval's theorem, the expected RMS of the response to a white noise input [33] this rating can be directly translated into an H_2 requirement[§]. The 2-norm of the weighted acceleration signal must not exceed 0.315 m/s^2 = 0.032 g for the best ride comfort rating ('not uncomfortable') [42]. The ratio of this limit (0.032 g) and the largest expected reference input (2‰c) is used as a constraint on the weighted RMS acceleration.

3. Limit on Elevator Commands

Saturation of the elevator deflection rate is prevented by constraining the H_∞ norm of the transfer function from the reference (δ_{LAD}^{ref}) to the elevator deflection rate ($\dot{\delta}_E$) by the ratio of elevator deflection rate limit (40 deg/s) and the largest expected reference input (2‰c).

V. Results

A. Performance of Individual Controllers

Algorithm 1 (page 12) is utilized to synthesize the baseline controller, while the MLA lift redistribution controller is synthesized without iterative procedure for both combined and individual LAD deflection. The continuous controller gain scheduling is implemented in the `systune` framework using `tunableSurfaces`. Tuned parameters resulting from the synthesis are documented in appendix Table 3 and visualized in appendix Figure 12. To provide insight into the control design, their performance is tested individually in this section: The FAS is tested with the MLA suppressed, and vice versa. While the controller synthesis relies on models with 75 states, the results of this section are based on full order linear models.

1. Nominal Performance of Baseline Controller

The ΔC^* handling quality criteria constitutes a guideline for the desirable time response of the aircraft when pilots apply some corrections and finely control the flight path. The tracking performance for $\Delta n_{z,feas}/3$ step inputs is shown

[§]Note that there is a certain mismatch between ISO 2631-1, which is related to the stochastic interpretation of the 2-norm, and the MLA lift redistribution that only receives step inputs, which are related with the deterministic interpretation of the 2-norm. The ISO 2631-1 is still used since there are no known ride-quality criteria on system responses to vertical acceleration step/impulse inputs.

in Figure 6 for linear systems throughout the flight envelope with MTOW and varying CG position. The feedforward controller outputs a large signal, such that the elevator is quickly deflected. This accelerates the system response, meeting the ΔC^* step response throughout. The elevator deflection is far below the saturation limit of 20 deg. Even though the elevator deflection rate constraint (see section IV.A.5) is applied to sinusoidal inputs for all frequencies up to the Nyquist frequency, the peak deflection rate is well below the saturation limit of 40 deg/s.

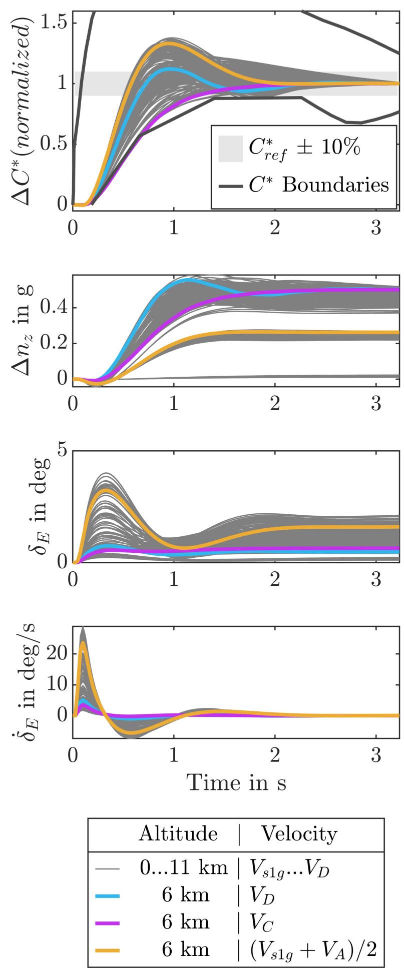

Fig. 6 Pull-up maneuver step response of baseline controller throughout the flight envelope with MTOW and varying CG in gray, three exemplary responses with decreasing dynamic pressure colored

In the very rare case that an aggressive maneuver is deemed necessary, the physical limits of the actuators and the need to avoid overstressing the airframe supersede the handling characteristics considerations. Since the simulation results in Figure 6 relate to only one third of the maximum load factor $\Delta n_{z,feas}$, the elevator actuator rate is expected to be saturated for $\Delta n_{z,feas}$ step inputs at some flight points with low dynamic pressure. In this work, a rate limiter is implemented at the elevator input which ensures that the elevator rate remains below the saturation limit at the expense of a slower tracking response for the edge-cases with low dynamic pressure.

2. Nominal Performance of MLA Lift Redistribution

The MLA lift redistribution controller is tested without FAS in horizontal flight. For this demonstration, $\delta_{E,FAS}$ is set to zero and a step signal is fed to δ_{LAD}^{tune}, cf. Figure 5.

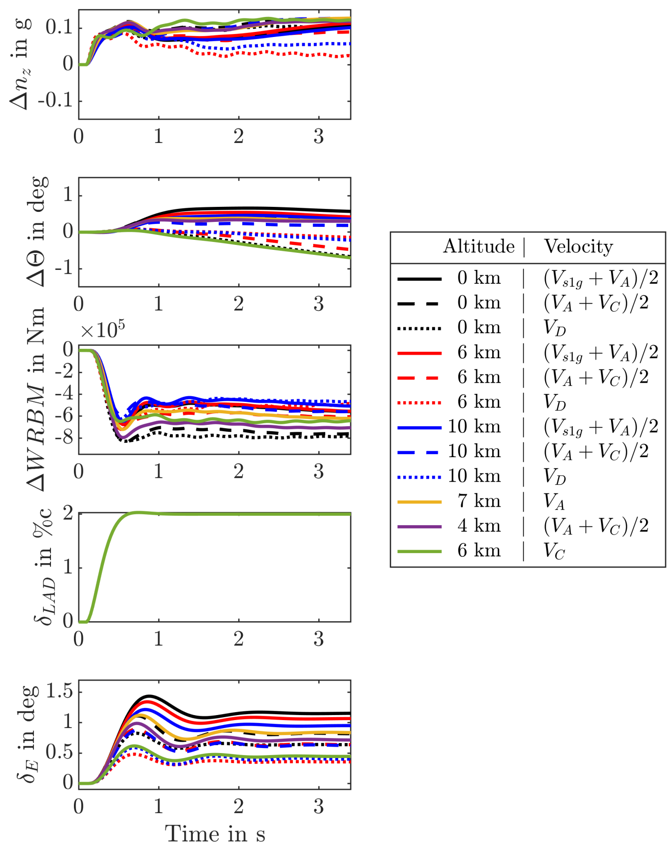

Fig. 7 Step response of lift redistribution controller in horizontal flight using all LAD sections for design flight points with MTOW and default CG position

The LAD deflection, commanded by $\boldsymbol{MLA_{LAD,reL}}$, reduces the outboard lift and also produces a pitch-up moment. This is compensated by a pitch-down elevator deflection (trailing edge down) commanded by $\boldsymbol{MLA_{E,reL}}(\boldsymbol{p})$, see Figure 7. Altogether, the lift redistribution has only a minor influence on the load factor and the pitch rate, so the MLA activation has little influence on the FAS. Therefore, the baseline controller is largely input-output decoupled from the MLA and the pilots are unlikely to notice a change in behavior due to the activation of the MLA function.

B. Performance of Combined Controllers

1. Worst Case Loads over Flight Envelope

In this section, the combined baseline controller and the MLA function are evaluated. Figure 8 shows the worst-case WRBM for pull-up maneuvers with $\Delta n_{z,feas}$ for all fight points (FP) and mass cases / CG positions (MC) using several indicators: one for each subplot. For all indicators, the absolute load responses L are considered and are obtained as the superposition of the trim loads L_{trim} and the incremental loads ΔL:

$$L(MC, FP, t) = \Delta L(MC, FP, t) + L_{trim}(MC, FP), \quad \forall (MC, FP, t) \tag{9}$$

The first performance indicator is the worst-case load at each flight point, considering peak load over time for each mass case individually and then selecting the highest peak load over all mass cases. This indicator is shown for the $noMLA$ case, i.e., inactive MLA, in Figure 8a

$$L_{max}^{noMLA}(FP) = \max_{MC}\left(\max_{t}\left(L^{noMLA}(MC, FP, t)\right)\right), \quad \forall FP \tag{10}$$

and the MLA, all case, i.e., with the MLA function active and using all LAD sections, in Figure 8b

$$L_{max}^{MLA,all}(FP) = \max_{MC}\left(\max_{t}\left(L^{MLA,all}(MC, FP, t)\right)\right), \quad \forall FP \tag{11}$$

The local relative load alleviation $L_{LA,local}^{MLA,all}(FP)$, i.e., the load reduction obtained with the MLA function (using all LAD) at each flight point, can be expressed as follows and is represented in percent in Figure 8c

$$L_{LA,local}^{MLA,all}(FP) = \frac{L_{max}^{MLA,all}(FP)}{L_{max}^{noMLA}(FP)} - 1 \quad \forall FP \tag{12}$$

Finally, the worst-case load obtained at each flight point with the MLA function (still all LAD considered) $L_{max}^{MLA,all}(FP)$ are compared to the worst-case load obtained without MLA over the entire flight envelope

$$L_{envelope}^{noMLA} = \max_{FP}\left(L_{max}^{noMLA}(FP)\right) \tag{13}$$

A local (i.e., for each flight point with MLA) relative margin with respect to the load envelope of the $noMLA$ configuration that was just introduced is defined below and visualized in percent in Figure 8d

$$L_{LA,margin}^{MLA,all}(FP) = \frac{L_{max}^{MLA,all}(FP)}{L_{envelope}^{noMLA}} - 1 \quad \forall FP \tag{14}$$

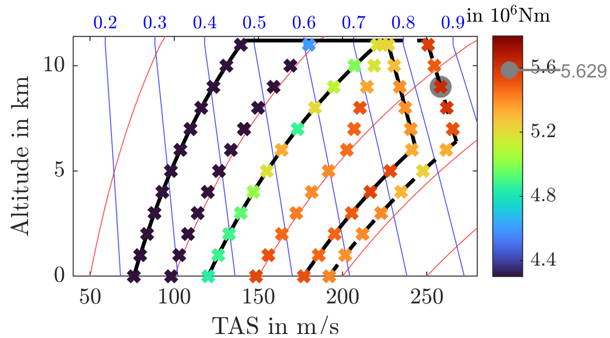

(a) Worst case loads without load alleviation (Eq. 10)

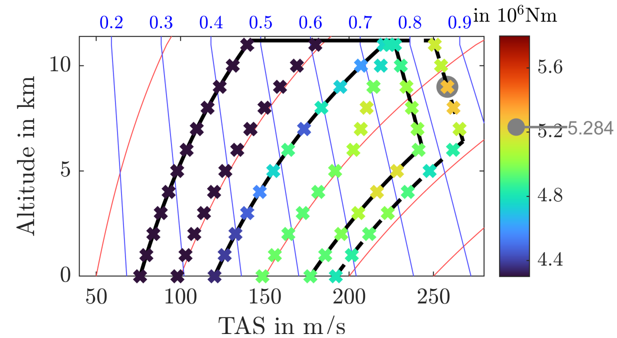

(b) Worst case loads with MLA using all LAD sections (Eq. 11)

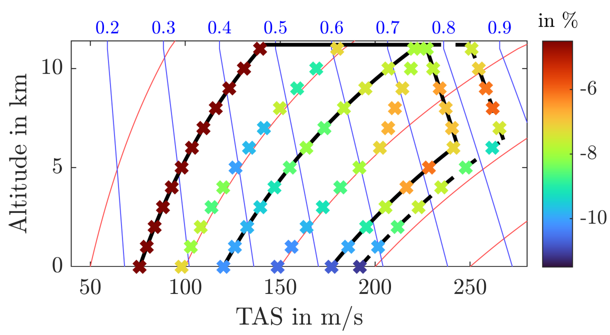

(c) Worst case loads with MLA using all LAD sections compared to the worst case loads without MLA at the same flight point (Eq. 12)

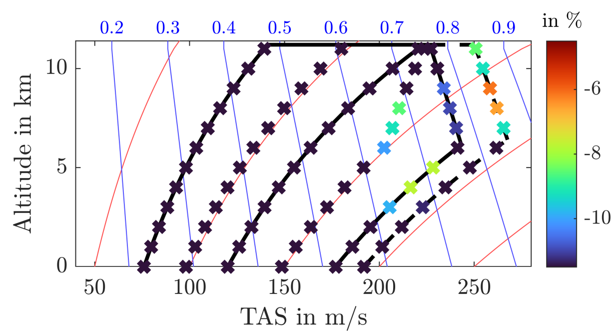

(d) Worst case loads with MLA using all LAD sections compared to the worst case loads without MLA for all flight points (Eq. 14)

Fig. 8 Worst case pull-up maneuver loads per flight point, three CG positions and two mass cases considered per flight point, distribution of WRBM over flight envelope, critical WRBM marked in gray

Large maneuver loads with and without MLA are at velocities beyond the maneuver velocity and all altitudes, see Figures 8a and 8b, since $\Delta n_{z,feas}$ is largest (2.5 g) at these flight points. The largest WRBMs occur at two disjoint regions in the flight envelope, i.e., at cruise speed V_C and for $H \in [4, 5]$ km as well as at dive velocity V_D and $H \in [8, 9]$ km, see Figures 8a, 8b and 8d. This is caused by the fact that the load factor transient response / overshoot varies over the flight envelope (cf. Figure 6 and Figure 7), and the pull-up maneuver and LAD deflection excite structural modes, such that the WRBM oscillates. The peak of this oscillation is synchronized with the load factor peak for the two disjoint regions with the largest WRBMs.

Overall, the critical WRBM (gray markers in Figures 8a and 8b) is alleviated by 6.5%. Figure 8c and Figure 7 indicate that the MLA performs best at high dynamic pressure and low Mach number. Note that for low altitude, the MLA effectiveness increases with EAS, while at high altitude, it decreases with EAS. This is due to the Mach number dependency of the micro-tab lift and moment coefficients.

2. Worst Case Loads over Wing Span

Figure 9a shows the worst case vertical bending M_x and torsion M_y moment for pull-up maneuvers with $\Delta n_{z,feas}$ for all fight points (FP) and mass cases / CG positions (MC) over the wing span. Critical mass cases are indicated by markers. The MTOW mass case is critical for the vertical bending moment, while both mass cases must be considered for the torsion moment. The maneuver load alleviation is conducted with the following wing actuator configurations: deactivated MLA ($noMLA$), use of individual LAD sections (MLA, out, MLA, mid, MLA, in), and simultaneous use of all actuators (MLA, all). As expected, using more LAD sections yields a larger decrease in maneuver loads. The incremental load envelopes are shown in Figure 9b. The incremental vertical bending moment envelope shows a continuous distribution, while the torsion moment envelope is discontinuous at the engine spanwise position (this is discussed at the end of this section). Figure 9c provides a relative comparison of active versus inactive load alleviation. A relative load alleviation regarding the worst case vertical bending moment

$$LA(M_x) = \frac{M_{x,envelope}^{MLA,all}}{M_{x,envelope}^{noMLA}} - 1 \quad \forall FP \tag{15}$$

of 6–13% is achieved across the wingspan using all LAD sections simultaneously. The vertical bending moment load alleviation is a superposition of the load alleviation from the individual LAD sections, and each LAD section contributes a similar amount to the combined vertical bending load alleviation up to 7 m semi-wingspan position. Their similar effectiveness is due to several opposing factors, e.g., the lever arm increases with a LAD positioned further out, but at the same time the local chord length and thus also the local change in lift is reduced.

The contributions of individual LAD sections deviate beyond the 7 m semi-wingspan position. This is due to the LAD deflection causing both a local lift decrease and an up-twisting moment. Hence, the wing beyond the LAD section is twisted upward (e.g., $LA(M_x)$ drops off first for the MLA, in case), resulting in different contributions of the individual LAD sections beyond the 7 m semi-wingspan position.

The load alleviation of the torsional bending moment $LA(M_y)$ at the outermost section of the wing (y >16 m) is zero for all actuator configurations, as the (time-) peak values occur before MLA activation. Further, at the outermost section of the wing, the load alleviation of the vertical bending moment $LA(M_x)$ is small or even positive for MLA with the inboard or midboard LAD sections. However, the outboard loads are not critical, as other constraints (e.g., manufacturing or flutter) may be driving the structural sizing. Note, that the wing structure has a very low torsional stiffness and an inherent bending-torsion coupling (the wingtip twists up to 10 deg down for the worst case maneuver load without load alleviation).

The earlier mentioned discontinuity in the incremental wing torsion envelope in Figure 9b is due to the large lever arm of the engines. For the MLA, all case the discontinuity is smaller since the MLA is over-actuated in this case[¶] and the critical load occurs at MLA activation. For all other LAD configurations, the critical load is synchronous with that of the $noMLA$ case, causing the discontinuities to have a similar size. Consequently, the discontinuity is only visible for the configuration MLA, all in Figure 9c. The same reason implies why the $LA(M_y)$ curve for simultaneous use of all LAD segments is not a superposition of the curves of the individual LAD segments.

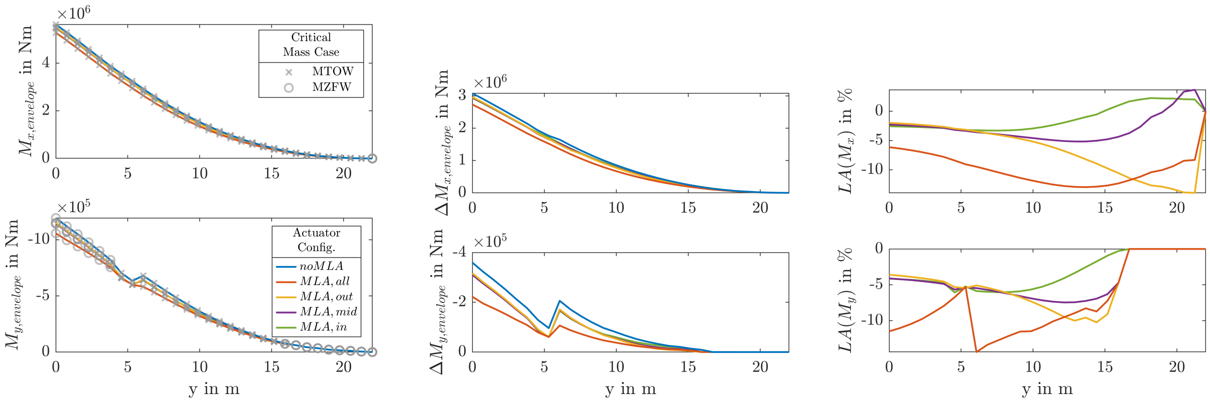

(a) Worst case loads for all flight points

(b) Worst case incremental loads for all flight points

(c) Worst case loads with MLA for all flight points compared to the worst case loads without MLA for all flight points (Eq. 15)

Fig. 9 Worst case pull-up maneuver loads, three CG positions and two mass cases considered per flight point, distribution over left wing in spanwise direction

C. Performance Enhancement

The (time-) peak values of the wing root vertical bending moment and load factor are shown in Figure 11a for MTOW, velocities above the maneuver speed, and three CG positions. There is a strong correlation between the WRBM and load factor (time-) peaks (correlation factor of 0.85 without MLA and 0.57 with MLA using all LAD sections), which was to be expected since the wing is loaded more as the load factor increases. Activating the MLA function decreases the WBRM (time-) peaks, while the load factor (time-) peaks are largely unaffected. Figure 11a also shows, as to be expected, an increase in load factor and WRBM overshoot for a rearward CG position.

In order to keep the tracking performance consistent regardless of the CG position, a CG-scheduling scheme is added in the following. Furthermore, an input filter is added to the baseline controller which reduces the load factor overshoot for sizing maneuvers. Note, that the critical mass case for the WRBM is MTOW, see Figure 9a, so only this mass case is considered.

[¶]Hence, for the given trigger logic, adding more LAD sections or employing more effective LADs would not decrease the wing torsion moment further than for the actuator configuration using all LAD sections. The load alleviation performance could be enhanced by an earlier MLA activation.

1. CG scheduling

It is well known that the static pitch stability of an aircraft with conventional configuration depends linearly on the CG position [43, Eq. 9.24]. Shifting the CG position rearward lowers the restoring moment ($C_{m,\alpha}$ becomes less negative), i.e., the aircraft becomes more agile. This implies for the given maneuvers that the load factor overshoot increases with a rearward CG shift, see Figure 11a. The effect is compensated by scaling the elevator deflection by

$$1 + K_{CG}^{P}(x_{CG} - x_{CG,Default})/MAC \tag{16}$$

with the CG-scheduling gain $K_{CG}^{P} = 8$ which is tuned manually such that the effect of the CG shift on the WRBM and load factor overshoot is minimized, see Figure 11b. Automatizing this procedure would certainly be possible and advisable on more complex problems, but the tuning is straightforward in the present case. By adding and progressively increasing this term, the load factor overshoot by aft CG and undershoot by forward CG gets progressively better up to the optimal value. A further increase of the gain would lead to an overcompensation, yielding increased WRBM and load factor overshoots for the forward CG position and vice-versa for the aft position - overall raising the critical WRBM. Adding the CG-scheduling law decreases the critical maneuver WRBM by 1.5% without MLA and by 1.3% with MLA using all LAD sections. The additional load alleviation may seem small, but a larger CG shift than 2%MAC may occur in reality, leading to a larger benefit. Furthermore, decoupling the aircrafts pitch dynamic from the CG position supports the pilot.

2. Baseline input filter

With CG-scheduling, the load factor overshoot is less than 10%. Recall that the 10% overshoot constraint relates to normal operation, i.e., to maneuvers with small load factor changes (cf. Section IV.A), where some overshoot is desired to fulfill the ΔC^* step response limits. For sizing maneuvers, however, the load factor overshoot can be further reduced by adding a nonlinear input filter in between the pilot stick output and the n_z^{ref} input. The filter is defined as

$$\frac{(\Delta n_z^{stick} - \Delta n_z^{ref})NL(\Delta n_z^{ref})T_s}{z-1} \tag{17}$$

where the nonlinear function $NL(\Delta n_z^{ref})$ is large[‖] for normal operation (Δn_z^{ref} <0.5 g), so that the filter rapidly converges to its input Δn_z^{stick}. For larger load factor changes, however, $NL(\Delta n_z^{ref})$ is small, see Figure 10. This results in a very quick initial reaction of Δn_z^{ref}, and above 0.5 g, the filter converges slowly to its input, reducing the load factor overshoot as well as the critical WRBM, see Figure 11c. Adding both the CG-scheduling and input filter laws decreases the critical maneuver WRBM by 3.3% without MLA and by 3.4% with MLA using all LAD sections.

[‖]Rearranging the filter transfer function 17 reveals that the filter reduces the remaining difference of Δn_z^{stick} and Δn_z^{ref} by $NL(\Delta n_z^{ref})T_s$ per time step. Hence setting $NL(\Delta n_z^{ref})$ to $T_s/2$ causes the filter to output 93.75% of the stick value within four time steps (for a step input), which is equivalent to 0.1s. Note that setting $NL(\Delta n_z^{ref})$ to T_s causes the filter to behave like a feed-through with unit delay.

Appendix Figure 13 provides further insight into the effects of the performance enhancements on the time response. The CG-scheduling leads to a more consistent time response regarding variations of the CG-position and the input filter reduces the load factor and wing root bending moment overshoot at the expense of a slightly slower response.

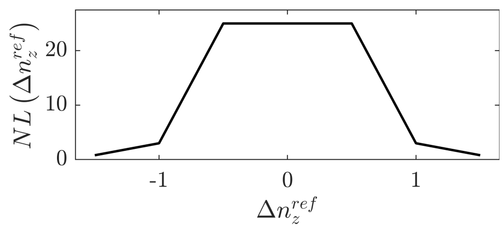

Fig. 10 Nonlinear input filter function definition

The use of an MLA function based on local lift reduction on the portions of the wing necessarily induces a reduction of the maximum load factor achievable in a steady state pitching maneuver from a pure aerodynamic point of view. In parts of the flight envelope, typically at lower dynamic pressure, the maximum achievable steady load factor is below the 2.5 g upper bound value defined in the certifications specifications §CS25.143. Unless it is disabled in these portions of the flight envelope (which would add failure cases to consider), the deployment of such MLA function induces a reduction of the aerodynamically achievable load factor during steady pitching maneuver. For the sake of the example, the aircraft without MLA could potentially reach 2.4 g and with MLA only 2.3 g. As long as the maneuverability of the aircraft is satisfying, this could be tolerated, cf. [1, §143 l]. Note that the formulation of these criteria has evolved in the last years, see for instance [44].

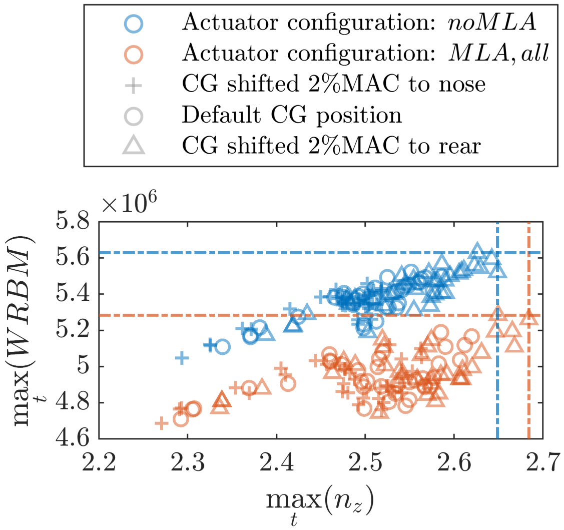

(a) Without CG-scheduling and input filter

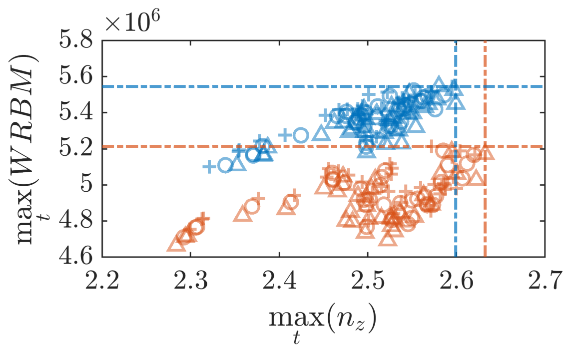

(b) With CG-scheduling

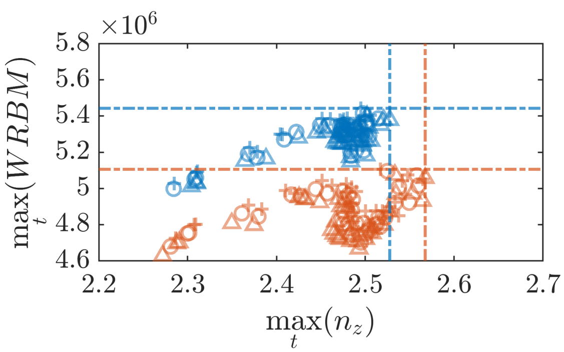

(c) With CG-scheduling and input filter

Fig. 11 (Time-) peak values of WRBM and load factor per flight point for MTOW, velocities above maneuver speed and three CG positions

VI. Conclusion

Two automated controller design approaches are presented for the synthesis of a baseline load factor / C^*-based control law and of a maneuver load alleviation function. The aim of these automated processes is twofold:

1) support (pre-)design studies through automatic adjustment of these controllers during the design loop, and

2) potentially serve as starting point for fine tuning of such functions by a control specialist.

The controller parameters for the elevator deflection of both laws are scheduled via a quadratic function of the equivalent airspeed and Mach number. The automatically tuned scheduling enables them to achieve their objectives across the entire flight envelope.

The considered actuators for load alleviation are micro-tabs and, like spoilers, work by reducing the local lift through flow separation on the upper surface of the wing. A decrease of the outboard lift is used to alleviate the inboard vertical bending moment. In this regard, the following strategy is proposed:

1) A second-order dynamic lift redistribution controller for maneuver load alleviation (MLA) which is tuned so that unnecessary excitation of the wing modes and unnecessary trajectory deviations are avoided during (de)activation.
2) An asymmetric (de)activation behavior of the load alleviation device (LAD) (different thresholds for activation and deactivation and an additional delay before deactivation) is used to prevent potential buffeting effects and any undesirable coupling with the structure.

The pull-up maneuver evaluations, conducted throughout the flight envelope with mass case and center of gravity (CG) variations, showed that, using all micro-tab sections simultaneously, the designed MLA decreased the vertical bending maneuver load envelope by 6 to 13% over the wingspan. For the inboard portion of the wing, each micro-tab section were found to be similarly effective. The worst-case torsion moments were also decreased. To further enhance the MLA performance, we propose:

1) scheduling the gains linearly with the CG position for a more consistent tracking behavior and to reduce the critical load, and
2) adding a nonlinear filter on the baseline controller input, which is tuned manually such that the (time-) peak wing root bending moment and load factor are decreased.

Adding both the CG scheduling and input filter yielded a reduction of the critical maneuver wing root bending moment by a further 3.3% without MLA and by 3.4% with MLA using all LAD sections.

Except for the performance enhancement mentioned above, the combined control design of the baseline and MLA function is fully automated. These enhancements could easily be integrated in the automated design loop. The controller design methodology worked reliably in all of the cases considered. Thus, we expect that it can be used successfully within an aircraft multidisciplinary optimization loop.

Acknowledgments

We would like to acknowledge the funding by the Deutsche Forschungsgemeinschaft (DFG, German Research Foundation) under Germany´s Excellence Strategy – EXC 2163/1 - Sustainable and Energy Efficient Aviation – Project-ID 390881007.

References

[1] EASA, "CS-25: Certification Specifications and Acceptable Means of Compliance for Large Aeroplanes," , 2023. Amendment 27, European Union Aviation Safety Agency.

[2] Allison, R. L., Perkin, B. R., and Schoenmann, R. L., "Application of winglets and/or wing tip extensions with active load control on the Boeing 747," Tech. Rep. 19780021107, NASA. Langley Research Center CTOL Transport Technologies, 1978. `https://ntrs.nasa.gov/citations/19780021107`.

[3] White, R. J., "Improving the Airplane Efficiency by Use of Wing Maneuver Load Alleviation," *Journal of Aircraft*, Vol. 8, No. 10, 1971, pp. 769–775. https://doi.org/10.2514/3.59169.

[4] Johnston, J. F., "Accelerated development and flight evaluation of active controls concepts for subsonic transport aircraft," Tech. Rep. 19820007204, NASA Contractor Report, 1982.

[5] Wallace, C., and Fezans, N., "Lidar-based Gust Load Alleviation - Results Obtained on a Generic Long Range Aircraft Configuration," *CEAS – EUCASS Aerospace Europe Conference 2023*, 2023. https://doi.org/10.13009/EUCASS2023-564.

[6] Cavaliere, D., and Fezans, N., "A Practical Approach to Automated Multiobjective Gust Load Alleviation Control Design in a structured H_2 / H_∞ Framework," 2024. CEAS-GNC-2024-042.

[7] Fournier, H., Massioni, P., Tu Pham, M., Bako, L., Vernay, R., and Colombo, M., "Robust Gust Load Alleviation of Flexible Aircraft Equipped with Lidar," *Journal of Guidance, Control, and Dynamics*, Vol. 45, No. 1, 2022, pp. 58–72. https://doi.org/10.2514/1.G006084.

[8] Bussemaker, "Wing Optimization With Active Load Control," Master's thesis, Technical University Delft and Airbus Aeromechanics Systems, 2018. http://resolver.tudelft.nl/uuid:099604d8-c056-471c-b003-e31605523074.

[9] Handojo, V., "Contribution to Load Alleviation in Aircraft Predesign and Its Influence on Structural Mass and Fatigue," Phd thesis, Technical University Berlin, 2020. https://elib.dlr.de/139558/.

[10] Wunderlich, T. F., Dähne, S., Reimer, L., and Schuster, A., "Global Aerostructural Design Optimization of More Flexible Wings for Commercial Aircraft," *Journal of Aircraft*, Vol. 58, No. 6, 2021, pp. 1254–1271. https://doi.org/10.2514/1.C036301.

[11] Pereira, M., Kolmanovsky, I., Cesnik, C., and Vetrano, F., "Model Predictive Control for Maneuver Load Alleviation in Flexible Airliners," *IFASD 2019*, 2019.

[12] Krengel, M., "Basic Maneuver Load Alleviation in Conceptual Aircraft Design," *22th ONERA-DLR Aerospace Symposium*, 2022. https://elib.dlr.de/186721/.

[13] Favre, C., "Fly-by-wire for commercial aircraft: the Airbus experience," *International Journal of Control*, Vol. 59, No. 1, 1994, pp. 139–157. https://doi.org/10.1080/00207179408923072.

[14] Delannoy, S., and Oudin, S., "Longitudinal control law for modern long range civil aircrafts," *EuroGNC 2nd CEAS Specialist Conference on Guidance, Navigation & Control*, 2013. https://aerospace-europe.eu/media/books/delft-0027.pdf.

[15] Harris, J. J., "F-35 Flight Control Law Design, Development and Verification," *2018 Aviation Technology, Integration, and Operations Conference*, 2018. https://doi.org/10.2514/6.2018-3516.

[16] Puyou, G., Bérard, C., Ferreres, G., and Menard, P., "Conception multi-objectif de lois de pilotage pour un avion de transport civil," *Journal Europeen des Systemes Automatises*, Vol. 40, No. 1, 2006. https://doi.org/10.3166/jesa.40.1019-1051.

[17] Guinn, W. A., Rising, J. J., and Davis, W. J., "Development of an Advanced Pitch Active Control System for a Wide Body Jet Aircraft," Tech. Rep. 19870008280, NASA Contractor Report, 1984. https://ntrs.nasa.gov/citations/19870008280.

[18] Berger, T., Tischler, M., Hagerott, S. G., Cotting, M. C., Gresham, J., George, J., Krogh, K., D'Argenio, A., and Howland, J., "Handling Qualities Flight Test Assessment of a Business Jet NzU P-beta Fly-By-Wire Control System," *2017 AIAA Atmospheric Flight Mechanics Conference / SciTech Forum*, 2017. https://doi.org/10.2514/6.2017-1398.

[19] Delannoy, S., "Airbus Generic Control Laws," *Proceedings of the 2019 CEAS EuroGNC conference*, 2019. CEAS-GNC-2019-065.

[20] Pérez, C. A., Theodoulis, S., Sève, F., and Goerig, L., "Automatic weighting filter tuning for robust flight control law design," *IFAC 18th IFAC Workshop on Control Applications of Optimization*, Vol. 55, No. 16, 2022, pp. 400–405. ISSN 2405-8963, https://doi.org/10.1016/j.ifacol.2022.09.057.

[21] Strohteicher, T., and Fezans, N., "Automated Tuning of a Baseline Flight Control System with Maneuver Load Alleviation for an Energy-Efficient Passenger Airplane," *IFASD 2024*, 2024.

[22] Karpuk, S., Radespiel, R., and Elham, A., "Assessment of Future Airframe and Propulsion Technologies on Sustainability of Next-Generation Mid-Range Aircraft," *Aerospace*, Vol. 9, No. 5, 2022. ISSN 2226-4310, https://doi.org/10.3390/aerospace9050279.

[23] Beyer, Y., Cavaliere, D., Bramsiepe, K., Khalil, K., Bauknecht, A., Fezans, N., Steen, M., and Hecker, P., "An Aeroelastic Flight Dynamics Model for Gust Load Alleviation of Energy-Efficient Passenger Airplanes," *AIAA AVIATION 2023 Forum*, 2023. https://doi.org/10.2514/6.2023-4452.

[24] Waszak, M. R., and Schmidt, D. K., "Flight dynamics of aeroelastic vehicles," *Journal of Aircraft*, Vol. 25, No. 6, 1988, pp. 563–571. https://doi.org/10.2514/3.45623.

[25] Khalil, K., Asaro, S., and Bauknecht, A., "Active Flow Control Devices for Wing Load Alleviation," *Journal of Aircraft*, Vol. 59, No. 2, 2022, pp. 458–473. https://doi.org/10.2514/1.C036426.

[26] Geisbauer, S., "Numerical Simulation and Validation of Aerodynamics of Static and Dynamic Spoilers," *Journal of Aircraft*, Vol. 58, No. 6, 2021, pp. 1187–1203. https://doi.org/10.2514/1.C036145.

[27] Maboy, D., "Experimental Methods to Determine Control Effectiveness in Wind Tunnels," *AGARD Special Course on Aerodynamic Characteristics of Controls*, Vol. 711, 1983.

[28] Stevens, B., Lewis, F., and Johnson, E., *Aircraft Control and Simulation*, 3rd ed., Wiley & Sons, New Jersey, 2016. ISBN 978-1-118-87098-3.

[29] Boiffier, J.-L., *The Dynamics of Flight: The Equations*, Wiley & Sons, New York, 2000. ISBN 978-0-470-86052-6.

[30] Leishman, J. G., "Unsteady lift of a flapped airfoil by indicial concepts," *Journal of Aircraft*, Vol. 31, No. 2, 1994, pp. 288–297. https://doi.org/10.2514/3.46486.

[31] MathWorks, "Control System Toolbox R2023b," Tech. rep., The MathWorks, Inc., 2023.

[32] Apkarian, P., and Noll, D., "The H_∞ Control Problem is Solved," *Aerospace Lab*, Vol. 13, No. 1, 2017. https://doi.org/10.12762/2017.AL13-01.

[33] Skogestad, S., and Postlethwaite, I., *Multivariable Feedback Control: Analysis and Design*, 2nd ed., New York: Wiley & Sons, 2005. ISBN 978-0-470-01167-6.

[34] Sutherland, J. P., "Fly-By-Wire Flight Control Systems," , 1968. Air Force Flight Dynamics Lab Wright-Patterson AFB OH. https://apps.dtic.mil/sti/citations/AD0679158.

[35] Field, E., *The Application of a C Flight Control Law to Large Civil Transport Aircraft*, College of Aeronautics report, College of Aeronautics, Cranfield Institute of Technology, 1993. ISBN 978-1-871564-58-7.

[36] Puyou, G., "Conception multi-objectifs de lois de pilotage pour un avion de transport civil," Phd thesis, Institut Supérieur de l'Aéronautique et de l'Espace, 2005.

[37] Seiler, P., Packard, A., and Gahinet, P., "An Introduction to Disk Margins," *IEEE Control Systems Magazine*, Vol. 40, No. 5, 2020. https://doi.org/10.1109/MCS.2020.3005277.

[38] Berger, T., Tischler, M., Hagerott, S., Gangsaas, D., and Saeed, N., "Longitudinal Control Law Design and Handling Qualities Optimization for a Business Jet Flight Control System," *AIAA Atmospheric Flight Mechanics Conference*, 2012. https://doi.org/10.2514/6.2012-4503.

[39] Blanken, C., Tischler, M., Lusardi, J., Berger, T., Ivler, C., and Lehmann, R., "Proposed Revisions to Aeronautical Design Standard-33E (ADS-33E-PRF) toward ADS-33F-PRF," , 2019. Special Report FCDD-AMV-19-01 https://apps.dtic.mil/sti/pdfs/AD1080657.pdf.

[40] Hahn, K.-U., and König, R., "ATTAS Flight Test and Simulation Results of the Advanced Gust Management System LARS." *Proceedings of the AIAA Atmospheric Flight Mechanics Conference*, 1992. https://doi.org/10.2514/6.1992-4343.

[41] Zuo, L., and Nayfeh, S. A., "Low order continuous-time filters for approximation of the ISO 2631-1 human vibration sensitivity weightings," Vol. 265, No. 2, 2003, pp. 459–465. ISSN 0022-460X, https://doi.org/10.1016/S0022-460X(02)01567-5.

[42] Kubica, F., and Madelaine, B., "Passenger Comfort Improvement by Integrated Control Law Design," *RTO AVT Specialists' Meeting on Structural Aspects of Flexible Aircraft Control*, RTO MP-36, 1990.

[43] Schmidt, D., *Modern Flight Dynamics*, 1st ed., New York: McGraw-Hill, 2011. ISBN 978-1-62410-616-3.

[44] EASA, "Electronic Flight Control Systems – Normal Load Factor Limiting System," , 2021. Final Equivalent Safety Finding ref. ESF-B25.143-01.

Appendix A: Tuned Controller Parameters

Table 3 Tuned Parameters

Parameter	p_0	p_{EAS}	p_{EAS2}	p_{Ma}	p_{Ma2}
		Baseline Controller			
$K^{FF}(\boldsymbol{p})$	3.0203	-3.7505	2.7619	-2.6821	2.0129
$K^{I}_{n_z}(\boldsymbol{p})$	2.9466	-1.2411	1.1566	-2.4903	1.7127
$K^{P}_{n_z}(\boldsymbol{p})$	1.2415	-2.6273	2.106	-1.048	1.1813
$K^{P}_{q}(\boldsymbol{p})$	0.5902	-0.3149	0.2002	-0.1325	0.0158
		MLA lift redistribution controller (using all LAD sections)			
$mag_{E,MLA}(\boldsymbol{p})$	0.3603	-0.0776	0.0344	-0.1288	-0.0246
$\omega_{n,E,MLA}(\boldsymbol{p})$	6.0579	0.5445	-0.255	0.2585	-0.03
$\zeta_{E,MLA}(\boldsymbol{p})$	0.2729	-0.0089	0.0766	-0.0459	-0.0082
		MLA lift redistribution controller (using outer LAD section)			
$mag_{E,MLA}(\boldsymbol{p})$	0.1351	-0.0266	0.0182	-0.0513	-0.0079
$\omega_{n,E,MLA}(\boldsymbol{p})$	6.9305	0.748	-0.5917	-0.0294	0.0972
$\zeta_{E,MLA}(\boldsymbol{p})$	0.2935	0.0858	0.0835	0.035	0.0271

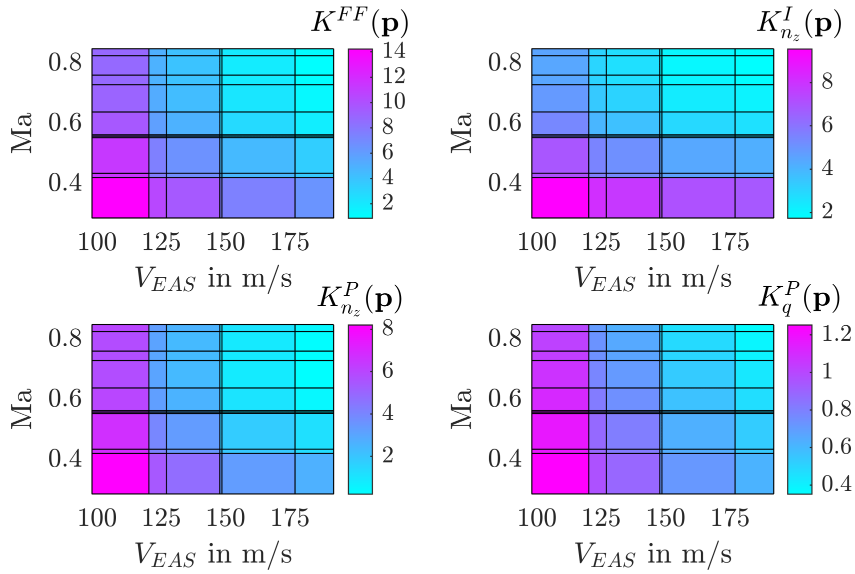

Fig. 12 Tuned gain surfaces of the baseline controller

Appendix B: Time Domain Response with Performance Enhancements

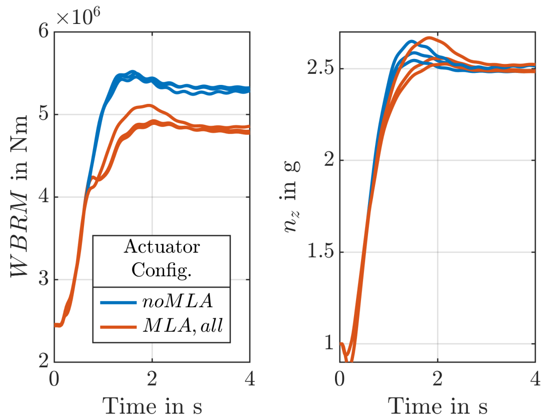

(a) Without CG-scheduling and input filter

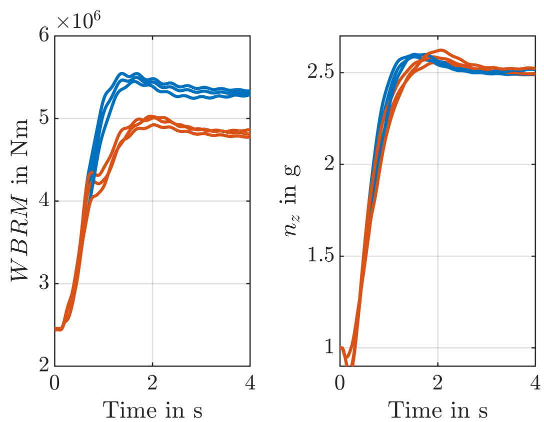

(b) With CG-scheduling

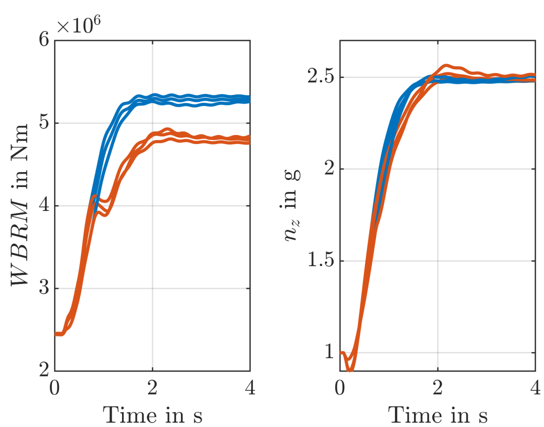

(c) With CG-scheduling and input filter

Fig. 13 Effects of the CG-scheduling and input filter on the time-responses of the flight points with largest n_z without CG-scheduling and input filter (MTOW, three CG positions)